

Composition-Dependent Plasmon-Enhanced Emission in Lead-Free $\text{Cs}_3\text{Cu}_2\text{X}_5$ Halides: A DFT–FDTD Study

Shoumik Debnath^a, Sudipta Saha^a, Khondokar Zahin^a, Ying Yin Tsui^b,
and Md. Zahurul Islam^{a,*}

^aDepartment of Electrical and Electronic Engineering,
Bangladesh University of Engineering and Technology, Dhaka 1000, Bangladesh

^bDepartment of Electrical and Computer Engineering,
University of Alberta, Edmonton, AB T6G 2H5, Canada

*Corresponding author. E-mail: mdzahurulislam@eee.buet.ac.bd

Abstract

Lead-free $\text{Cs}_3\text{Cu}_2\text{X}_5$ ($X = \text{Cl}, \text{Br}, \text{I}$) halides show high photoluminescence quantum yields (PLQY) and good ambient stability, yet LEDs based on these materials still suffer from poor optical outcoupling. In this work, we combine density functional theory (DFT) and finite-difference time-domain (FDTD) simulations to optimize plasmonic enhancement in $\text{Cs}_3\text{Cu}_2\text{X}_5$ LEDs using composition-specific optical constants. First-principles calculations provide wavelength-dependent refractive index and extinction coefficient data for each halide. These values are then used in FDTD to model a complete device stack with Ag/SiO₂ core-shell nanostructures. Out of the three halides, $\text{Cs}_3\text{Cu}_2\text{Cl}_5$ performs best with $4.4\times$ Purcell enhancement and 30% light extraction using optimized nanorods. The chloride outperforms the others due to its lower refractive index ($n \approx 1.9$). $\text{Cs}_3\text{Cu}_2\text{Br}_5$ has the highest spectral overlap (95.5%) but only moderate extraction efficiency (26%) because of increased optical confinement. $\text{Cs}_3\text{Cu}_2\text{I}_5$ requires a nanosphere geometry and shows limited performance (10% extraction) despite reasonable Purcell enhancement. Distance-dependent analysis shows that optimal emitter-plasmon separation varies with composition, ranging from 8–12 nm for $\text{Cs}_3\text{Cu}_2\text{Br}_5$ to approximately 15 nm for $\text{Cs}_3\text{Cu}_2\text{Cl}_5$. These results provide composition-specific design guidelines for plasmon-enhanced lead-free LEDs.

1 Introduction

Metal halide perovskite LEDs have advanced rapidly over the past decade. Red emitters now hit 28% external quantum efficiency (EQE) [1], green devices reach 30% [2], and blue recently crossed 23% [3]. These numbers rival state-of-the-art OLEDs.[4, 5] The performances are achieved due to high absorption coefficients, tunable emission across visible to near-infrared wavelengths, narrow linewidths below 20 nm, and high photoluminescence quantum yields.[6, 7, 8] However, two fundamental problems remain. First, lead toxicity blocks commercialization.[9, 10, 11] Second, even high-yield emitters lose roughly 80% of

generated photons to waveguide and substrate modes.[12, 13, 14] Simply replacing lead will not solve the photon extraction bottleneck.

Early lead-free efforts targeted tin and germanium perovskites because Sn^{2+} and Ge^{2+} mimic the Pb^{2+} valence configuration.[9, 15] Tin-based PeLEDs have reached EQEs near 20%.[7] But both cations oxidize rapidly to tetravalent states under ambient conditions, creating deep-level defects that kill emission within hours.[7, 9, 16] Tin is especially unstable due to its low $\text{Sn}^{2+}/\text{Sn}^{4+}$ redox potential of +0.15 V.[16] For commercial viability, devices need to operate beyond 10,000 hours.[17] Neither lead-based nor current lead-free systems meet this requirement alongside cost and safety constraints.

The optical extraction problem persists regardless of the emitter material. Halide perovskites have refractive indices around 2.5,[4, 14, 18] which limits outcoupling efficiency to roughly 8%.[4] Total internal reflection alone accounts for about 56% of radiative power loss.[13, 14] Fixing these losses requires accurate wavelength-dependent optical constants, specifically the refractive index (n) and extinction coefficient (k), which vary with composition and emission energy.[19, 20] Most optical models use generic n and k datasets that cause spectral mismatch between photoluminescence and cavity resonances.[19, 21] Without composition-specific dispersion data, device optimization remains empirical rather than predictive.

These challenges share a common root. Material development and photonic engineering have been treated as separate problems.[22] Synthetic chemists optimize composition for stability without comprehensive optical characterization.[23] Device engineers use placeholder optical constants that may not match the actual material.[24] The result is incomplete solutions. Materials that resist degradation can still suffer from poor photon extraction. High-PLQY emitters placed in optically mismatched environments underperform. Real progress requires tackling both issues together.

Copper-based halides with the $\text{Cs}_3\text{Cu}_2\text{X}_5$ stoichiometry ($\text{X} = \text{Cl}, \text{Br}, \text{I}$) offer a promising path forward. Unlike conventional three-dimensional ABX_3 perovskites, $\text{Cs}_3\text{Cu}_2\text{X}_5$ has a zero-dimensional crystal structure consisting of isolated $[\text{Cu}_2\text{X}_5]^{3-}$ bi-octahedral dimers separated by cesium cations.[25, 26] This arrangement confines excitons to individual molecular units. The monovalent Cu^+ ($3d^{10}$) configuration provides a closed-shell electronic structure that resists oxidation, eliminating the instability pathways that plague Sn^{2+} and Ge^{2+} systems.[27, 28, 29] As a result, $\text{Cs}_3\text{Cu}_2\text{X}_5$ films maintain structural and optical integrity for weeks under ambient conditions without encapsulation.[26, 30] Recent work has reported PLQYs approaching 95%,[27, 31] with emission tunable from blue to near-infrared through halide substitution.[28, 32] $\text{Cs}_3\text{Cu}_2\text{Cl}_5$ emits blue-green around 440 to 520 nm,[31, 33] $\text{Cs}_3\text{Cu}_2\text{Br}_5$ emits green-yellow around 540 to 580 nm,[32] and $\text{Cs}_3\text{Cu}_2\text{I}_5$ emits in the green region around 530 to 550 nm.[28, 34] Strong electron-phonon coupling within the isolated dimers produces self-trapped excitons with broadband emission and large Stokes shifts around 200 to 600 meV.[27, 35] Still, PeLEDs using these materials show modest EQEs around 1 to 5%.[36] Chemical stability alone does not guarantee good device performance.

Addressing the optical extraction challenge requires computational methods that bridge material-scale dispersion and device-scale electromagnetics.[24] First-principles DFT calculations using hybrid functionals like HSE06 with spin-orbit coupling provide accurate band structures and dielectric functions.[37, 38] The resulting wavelength-dependent n and k spectra capture intrinsic material dispersion without relying on extrapolated values.[39] However, DFT describes bulk properties and cannot model electromagnetic field dynamics within multilayer device architectures.[25, 22] The FDTD method fills this

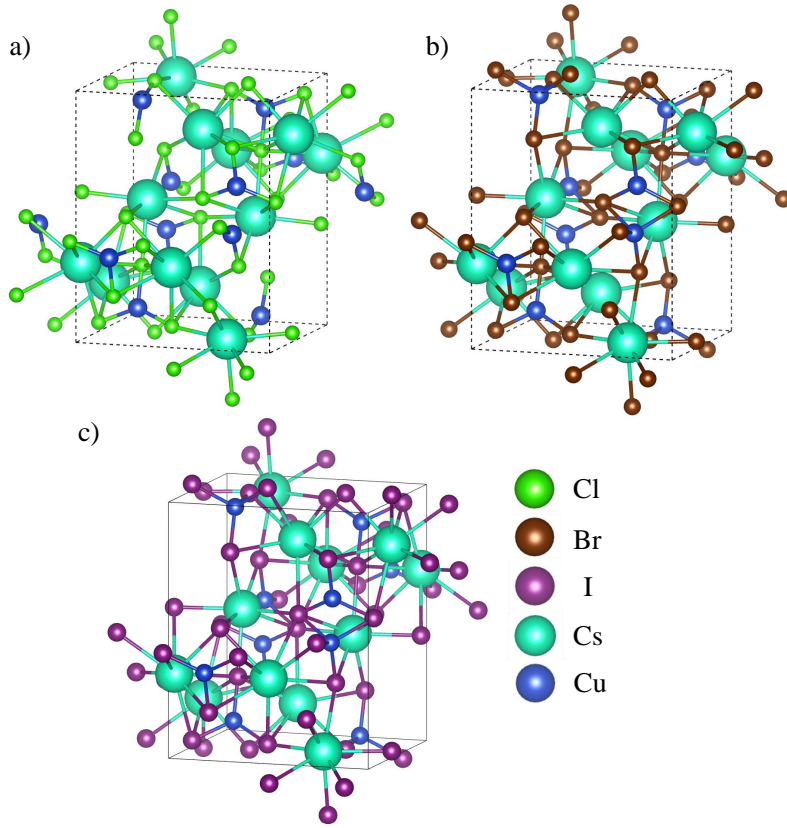


Figure 1: Crystal structure of $\text{Cs}_3\text{Cu}_2\text{X}_5$ (a) $\text{X} = \text{Cl}$, (b) $\text{X} = \text{Br}$, and (c) $\text{X} = \text{I}$. The green, brown, violet, sky blue, and blue atom colors correspond to Cl, Br, I, Cs, and Cu atoms, respectively.

gap by solving Maxwell's equations numerically in space and time.[14, 40] Importing DFT-derived optical constants into FDTD device models allows physically consistent evaluation of Purcell factor, light extraction efficiency, spectral overlap, and far-field profiles.[41]

Beyond passive optical engineering, plasmonic coupling through embedded metallic nanostructures offers active enhancement of light extraction.[12] Noble-metal nanoparticles support localized surface plasmon resonances that concentrate electromagnetic fields at the nanoscale and accelerate radiative recombination.[42] Gold nanorods combine excellent chemical stability with tunable plasmon resonances. Their longitudinal mode can be engineered through aspect-ratio control to align with $\text{Cs}_3\text{Cu}_2\text{X}_5$ emission, achieving strong spectral overlap and Purcell enhancement.[43, 44] But accurate design of plasmon-emitter coupling requires composition-specific optical constants to predict resonance alignment at the nanoscale.

Despite growing interest in lead-free perovskites, systematic studies linking halide composition, optical constants, and plasmonic performance remain scarce.[45] Prior research has mostly focused on structural stability or bandgap tuning for photovoltaics.[25] Most plasmonic simulations still use generalized n and k datasets, undermining the accuracy of enhancement predictions.[46] The quantitative connection between halide composition, optical dispersion, plasmon resonance alignment, and device-level performance has not been established for $\text{Cs}_3\text{Cu}_2\text{X}_5$ systems.[45]

Here, we develop a fully integrated DFT-FDTD framework that establishes quanti-

tative links between halide composition, wavelength-dependent optical properties, and plasmonic enhancement in $\text{Cs}_3\text{Cu}_2\text{X}_5$ -based PeLEDs. Composition-specific n and k spectra derived from DFT are directly implemented in FDTD simulations that model emission enhancement, nanorod-emitter coupling, and far-field radiation. We further optimize Ag-nanorod geometries to maximize light extraction efficiency (LEE), Purcell factor, and spectral overlap. This integrated approach combines the chemical stability of copper-based halides with engineered photonic control, providing a predictive design pathway from atomic composition to device-level light extraction.

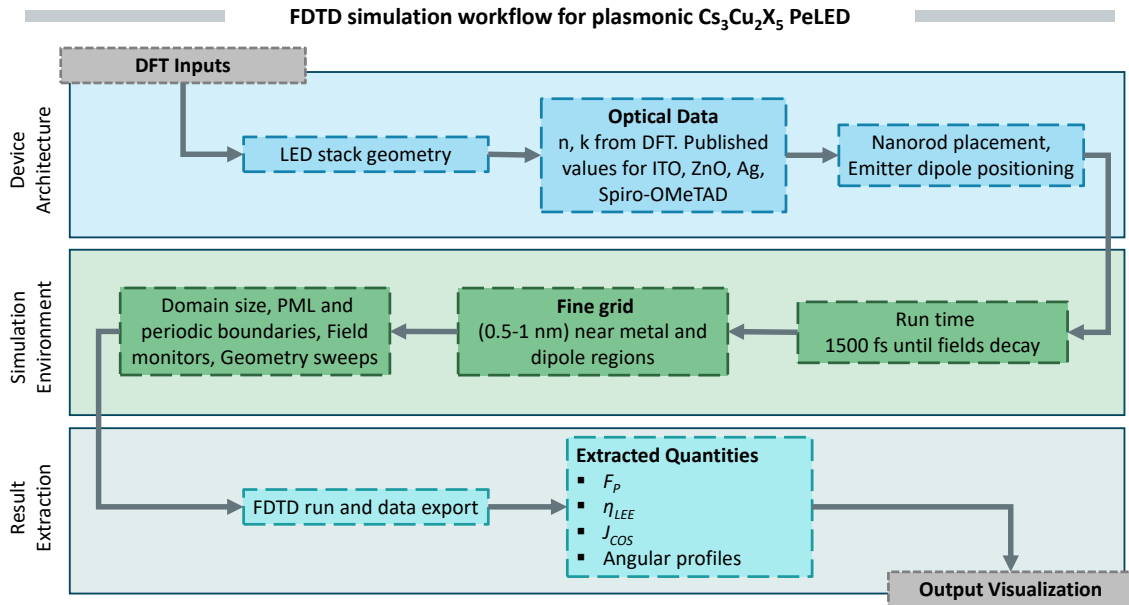


Figure 2: Overview of the DFT-FDTD modeling approach adopted in this work. Optical constants from first-principles calculations feed into device-level electromagnetic simulations that extract key performance metrics.

2 Methodology and Theoretical Background

2.1 DFT Methodology

We carried out all density functional theory calculations using the CASTEP code. We treated exchange-correlation effects with the PBE functional within the generalized gradient approximation framework. Ultrasoft pseudopotentials described the interactions between ions and electrons. We treated the following valence electron configurations explicitly: cesium $6s^1$, copper $3d^94s^2$, chlorine $3s^23p^5$, bromine $4s^24p^5$, and iodine $5s^25p^5$. We expanded the electronic wavefunctions using a plane-wave basis set with a kinetic energy cutoff of 450 eV. For Brillouin zone integration, we used a $6 \times 6 \times 6$ Monkhorst-Pack k-point grid.

We obtained starting structures from experimentally determined orthorhombic unit cells in the $Pnma$ space group. Each unit cell contained 40 atoms. We relaxed both lattice vectors and atomic positions for all three halide compositions using the BFGS optimization algorithm. We continued the relaxation until total energy changes dropped below $1 \times$

10^{-5} eV/atom, residual forces fell under 0.03 eV/Å, and atomic displacements stayed within 0.001 Å. These tight thresholds ensured well-converged ground state geometries.

After obtaining relaxed structures, we computed electronic band structures and density of states. We kept the same k-point mesh and smearing parameters from the ground state runs for consistency. We plotted band dispersions along the standard high-symmetry path for orthorhombic crystals, going through Γ , Z, Y, T, S, X, U, and R points in sequence. We set the Fermi level to zero energy in all plots. We then calculated optical properties from the frequency-dependent dielectric function. We evaluated the dielectric response for photon energies spanning 0 to 20 eV using the independent particle approximation. This approach captures interband transitions that govern absorption and refractive index behavior in the visible and ultraviolet ranges.

2.2 FDTD Simulation Setup

We modeled the optical behavior of plasmonic $\text{Cs}_3\text{Cu}_2\text{X}_5$ LEDs using three-dimensional FDTD simulations in Lumerical (Ansys Inc.).[47] Figure 2 shows the computational workflow.

We designed the device stack to match experimentally reported LED architectures.[48] Starting from the bottom, we used 100 nm of ITO as the anode. On top of that we placed a 35 nm Spiro-OMeTAD hole transport layer. The 50 nm $\text{Cs}_3\text{Cu}_2\text{X}_5$ active layer came next, followed by 40 nm of ZnO as the electron transport layer. A 100 nm Ag film served as the top cathode. We imported the refractive index and extinction coefficient spectra for each $\text{Cs}_3\text{Cu}_2\text{X}_5$ composition directly from our DFT results. For the other device layers, we used optical constants from published literature.[49, 50, 51]

We placed an electric dipole source inside the perovskite layer to represent spontaneous emission. The dipole radiated across visible wavelengths matching the photoluminescence range of $\text{Cs}_3\text{Cu}_2\text{X}_5$. We positioned this source a few nanometers away from the plasmonic nanostructure surface to capture near-field coupling effects.[52]

We chose boundary conditions to balance physical accuracy with computational efficiency. Along the lateral x and y directions, we applied periodic boundaries to simulate an extended array of emitters. In the vertical z direction, we used perfectly matched layers to absorb outgoing waves and prevent artificial reflections from the simulation edges.[53] We used a non-uniform spatial mesh throughout the simulation domain. We refined the grid spacing to 0.5–1 nm near the metal nanostructure and dipole region where field gradients are steepest. We increased the mesh spacing away from these areas to reduce memory use. We ran each simulation for 1500 fs, which gave the electromagnetic fields enough time to decay fully before we performed Fourier transforms to extract spectral data.

2.3 Plasmonic Nanostructure Design

We selected the nanoparticle geometry based on spectral overlap optimization between the localized surface plasmon resonance (LSPR) and the emission wavelength of each perovskite composition. Nanorods offer a tunable longitudinal plasmon mode through aspect-ratio control, making them suitable for targeting specific emission wavelengths. Nanospheres, in contrast, have a fixed dipolar resonance governed primarily by particle size and the surrounding dielectric environment. We evaluated both geometries for each $\text{Cs}_3\text{Cu}_2\text{X}_5$ variant and selected the structure with superior spectral alignment.

We positioned all nanostructures near the ZnO/perovskite interface (Fig. 4) with a

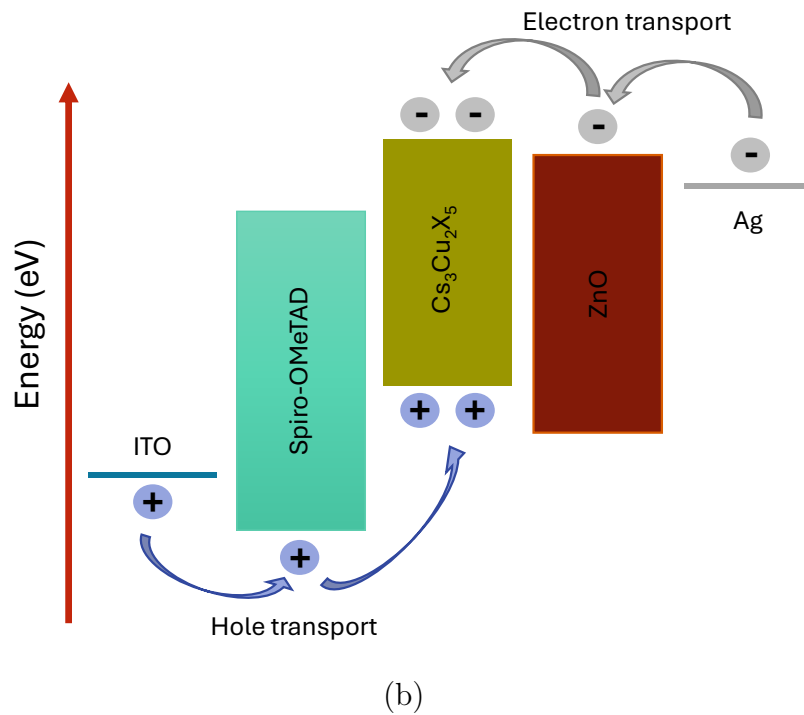
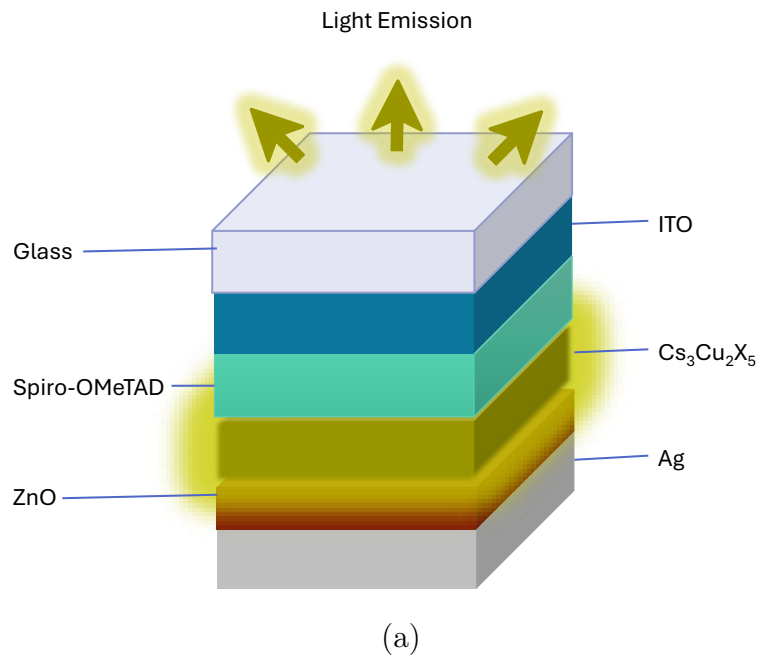


Figure 3: (a) Schematic of the simulated PeLED stack. (b) Energy band alignment showing hole injection from ITO through Spiro-OMeTAD and electron injection from Ag through ZnO into the perovskite active layer.

core-shell architecture. We fixed the SiO_2 shell thickness at 5 nm to position the emitter within the strong near-field enhancement regime while avoiding non-radiative energy transfer to the metal, which dominates below approximately 4 nm and leads to net quenching [54]. The shell also serves as a passivation layer to prevent charge carrier quenching. We used the Palik dataset for the frequency-dependent dielectric function of silver [50].

We optimized nanorod dimensions through parametric sweeps, varying the diameter from 8 to 25 nm and the length from 30 to 70 nm. We swept the nanosphere radius similarly to identify optimal coupling conditions. The optimization target was maximum spectral overlap between the LSPR and the composition-dependent emission peak of each $\text{Cs}_3\text{Cu}_2\text{X}_5$ variant.

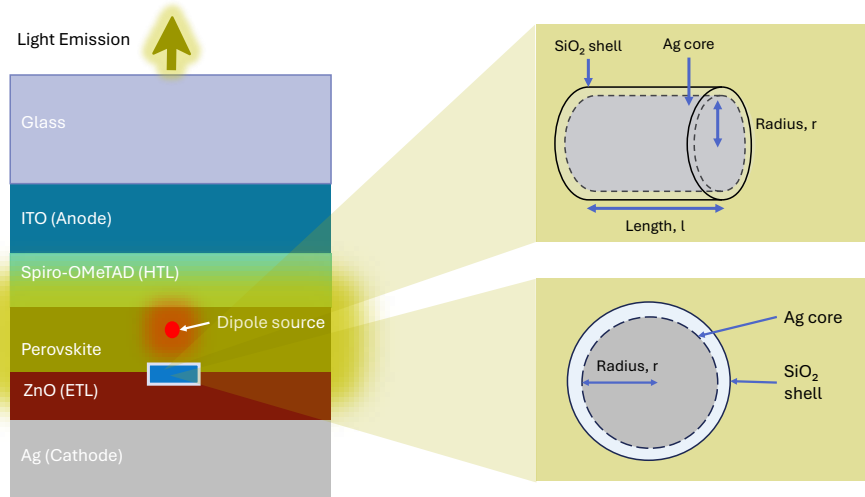


Figure 4: Placement of the dipole source and plasmonic nanostructures within the LED stack. A core-shell Ag/ SiO_2 nanorod (variable radius 8–25 nm, length 30–70 nm) is used for $\text{Cs}_3\text{Cu}_2\text{Cl}_5$ and $\text{Cs}_3\text{Cu}_2\text{Br}_5$, while a nanosphere geometry is employed for $\text{Cs}_3\text{Cu}_2\text{I}_5$. The 5 nm SiO_2 shell prevents non-radiative quenching while maintaining near-field coupling.

2.4 Compositional Analysis Strategy

We ran systematic simulations across the $\text{Cs}_3\text{Cu}_2\text{X}_5$ ($X = \text{Cl}, \text{Br}, \text{I}$) compositional series, both with and without the plasmonic nanostructure. For each halide composition, we used the corresponding DFT-derived n and k spectra in the FDTD model.

This dual-simulation approach isolates the influence of halide-induced optical dispersion changes from plasmonic coupling effects.[55] We normalized all extracted optical parameters to their non-plasmonic counterparts to determine the enhancement introduced by the nanostructure for each composition.

From the computed field data, we extracted Purcell factor, light extraction efficiency, near-field intensity distributions, and far-field angular patterns.

2.5 Performance Metrics

Purcell Factor. The Purcell factor (F_P) quantifies the enhancement of spontaneous emission rate when an emitter is placed in a modified photonic environment compared

to free space.[52] It arises from changes in the local density of optical states (LDOS) experienced by the dipole emitter. In FDTD simulations, F_P is calculated as the ratio of total power radiated by the dipole in the device structure (P_{cav}) to that in a homogeneous reference medium of equivalent refractive index (P_0)[47]

$$F_P = \frac{P_{cav}}{P_0} \quad (1)$$

This approach is valid because the emission rate is proportional to the LDOS, and the LDOS is proportional to the power emitted by the source. Values greater than unity indicate enhanced radiative recombination. Plasmonic nanostructures can produce large Purcell factors by concentrating electromagnetic fields near the emitter.[56]

LEE. The LEE represents the fraction of emitted photons that escape the device into the far field rather than being trapped by waveguide modes, substrate absorption, or total internal reflection.[57] LEE is defined as

$$\eta_{LEE} = \frac{P_{out}}{P_{total}} \quad (2)$$

where P_{out} is the power radiated into the upper hemisphere and P_{total} is the total power emitted by the dipole source. In FDTD simulations, P_{out} is calculated by integrating the Poynting vector over a far-field monitor placed above the device structure. High refractive index contrast at layer interfaces typically limits LEE in perovskite devices to below 20% without optical engineering.[14, 12] Plasmonic structures can redirect trapped modes into propagating radiation, thereby improving outcoupling. The LEE enhancement factor is defined as the ratio of LEE with and without the plasmonic nanostructure.

Spectral Overlap. Efficient plasmon-emitter coupling requires spectral alignment between the emitter photoluminescence and the LSPR of the nanostructure.[58] The degree of overlap determines the strength of near-field interaction and the magnitude of Purcell enhancement. To quantify spectral matching independent of amplitude, the cosine similarity metric (J_{cos}) is employed

$$J_{cos} = \frac{\int S(\lambda) C(\lambda) d\lambda}{\sqrt{\int S^2(\lambda) d\lambda} \sqrt{\int C^2(\lambda) d\lambda}} \quad (3)$$

where $S(\lambda)$ is the normalized emission spectrum and $C(\lambda)$ is the normalized plasmonic scattering cross-section spectrum. A value of $J_{cos} = 1$ indicates perfect spectral alignment and $J_{cos} = 0$ indicates no overlap. Nanostructure dimensions were optimized to maximize spectral overlap with the composition-dependent emission peaks of each $\text{Cs}_3\text{Cu}_2\text{X}_5$ variant.

Far-Field Radiation Pattern. The far-field angular distribution describes the directional characteristics of light emitted from the device.[59] It is computed by projecting the near-field data to the far-field regime through standard electromagnetic transformations involving Fourier transformation of the tangential electric field components recorded at the detection surface.[60] Directional emission concentrated within a narrow angular cone improves practical light collection and utilization. Plasmonic and cavity effects can reshape the far-field pattern, concentrating emission toward the surface normal.[61]

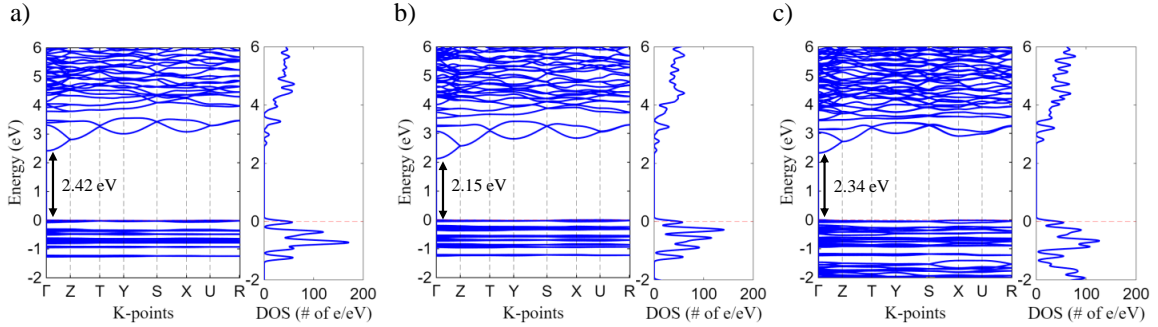


Figure 5: Calculated electronic band structures and total density of states (DOS) of $\text{Cs}_3\text{Cu}_2\text{X}_5$ compounds: (a) $\text{Cs}_3\text{Cu}_2\text{Cl}_5$, (b) $\text{Cs}_3\text{Cu}_2\text{Br}_5$, and (c) $\text{Cs}_3\text{Cu}_2\text{I}_5$. The band structures are plotted along the high-symmetry directions of the Brillouin zone, as indicated on the horizontal axis, with the Fermi level set to 0 eV (red dashed line). The corresponding total DOS is shown in the right panel of each subfigure. All compounds exhibit direct band gaps of 2.42 eV, 2.15 eV, and 2.34 eV for $\text{Cs}_3\text{Cu}_2\text{Cl}_5$, $\text{Cs}_3\text{Cu}_2\text{Br}_5$, and $\text{Cs}_3\text{Cu}_2\text{I}_5$, respectively, as marked in the band structure plots.

Table 1: Lattice parameters in the a , b , and c directions and band gaps E_g of $\text{Cs}_3\text{Cu}_2\text{X}_5$ materials.

Material	a (Å)	b (Å)	c (Å)	E_g (eV)	Remarks
$\text{Cs}_3\text{Cu}_2\text{Cl}_5$	9.57	10.74	13.41	2.42	This work
	9.18	10.51	13.14	2.45	Experimental[62]
	9.60	10.79	13.59	2.34	DFT[63]
$\text{Cs}_3\text{Cu}_2\text{Br}_5$	9.90	11.16	13.93	2.15	This work
	9.58	10.98	13.63	2.25	Experimental[64]
	9.92	11.19	13.92	2.09	DFT[63]
$\text{Cs}_3\text{Cu}_2\text{I}_5$	10.46	11.89	14.70	2.34	This work
	10.22	11.66	14.40	2.44	Experimental
	10.50	11.89	14.78	2.29	DFT[63]

3 Results and Discussion

3.1 Electrical and Optical Properties of $\text{Cs}_3\text{Cu}_2\text{X}_5$

Figure 5 shows the computed band structures and total density of states for all three $\text{Cs}_3\text{Cu}_2\text{X}_5$ compounds where X is Cl, Br, or I. We plotted band dispersions along high-symmetry paths in the Brillouin zone and set the Fermi energy to zero as a reference point. Each of the three materials behaves as a semiconductor with a direct band gap, meaning the valence band maximum and conduction band minimum occur at the same k -point.

For $\text{Cs}_3\text{Cu}_2\text{Cl}_5$ (Fig. 5a), a direct band gap of 2.42 eV is obtained. Upon substitution of Cl with Br (Fig. 5b), the band gap decreases to 2.15 eV. In the case of $\text{Cs}_3\text{Cu}_2\text{I}_5$ (Fig. 5c), the band gap slightly increases to 2.34 eV. The direct nature of the band gap is preserved across the halide series, indicating that both the conduction band minimum (CBM) and valence band maximum (VBM) occur at the same high-symmetry k -point.

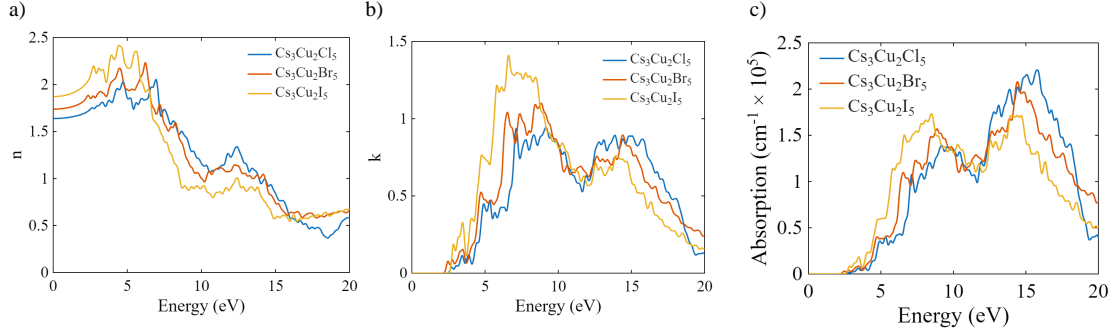


Figure 6: Optical properties of $\text{Cs}_3\text{Cu}_2\text{X}_5$ ($X = \text{Cl}, \text{Br}, \text{I}$): (a) n , (b) k , and (c) absorption coefficient as a function of photon energy. The calculated spectra are presented in the energy range of 0–20 eV for $\text{Cs}_3\text{Cu}_2\text{Cl}_5$, $\text{Cs}_3\text{Cu}_2\text{Br}_5$, and $\text{Cs}_3\text{Cu}_2\text{I}_5$. The absorption coefficient is expressed in cm^{-1} (scaled by 10^5). The distinct peak structures in n , k , and absorption originate from interband electronic transitions, reflecting the influence of halogen substitution on the optical response of the compounds.

The valence bands are flat near the VBM, which points to localized states from Cu– X orbital mixing. The conduction bands have more dispersion, so carriers should have more mobility in this region. The total DOS plots (right panels of Fig. 5) show clean band gaps with no mid-gap states.

Table 1 lists the optimized lattice parameters and band gaps. Calculated values for $\text{Cs}_3\text{Cu}_2\text{Cl}_5$ ($a = 9.57 \text{ \AA}$, $b = 10.74 \text{ \AA}$, $c = 13.41 \text{ \AA}$, $E_g = 2.42 \text{ eV}$) match well with experiments and earlier experimental and theoretical works. $\text{Cs}_3\text{Cu}_2\text{Br}_5$ comes out at $a = 9.90 \text{ \AA}$, $b = 11.16 \text{ \AA}$, $c = 13.93 \text{ \AA}$ with a 2.15 eV gap. $\text{Cs}_3\text{Cu}_2\text{I}_5$ has $a = 10.46 \text{ \AA}$, $b = 11.89 \text{ \AA}$, $c = 14.70 \text{ \AA}$ and a 2.34 eV gap, again matching the literature.

The lattice expands from Cl to Br to I as the halide ions get larger in size. Longer Cu– X bonds change the orbital overlap and shift the band gaps across the series. Overall, the structural and electronic properties obtained in this work demonstrate strong consistency with experimental and previously reported DFT results, confirming the reliability of the computational methodology employed. The optical absorption coefficient is fundamentally linked to the complex dielectric function, expressed as $\epsilon = \epsilon_1 + i\epsilon_2$. The imaginary component, ϵ_2 , can be determined by examining interband transitions within the electronic band structure, yielding the following relation [65]:

$$\epsilon_2(q \rightarrow 0_{\hat{u}}, \hbar\omega) = \frac{2e^2\pi}{\Omega\epsilon_0} \sum_{k,v,c} |\langle \Psi_k^c | \mathbf{u} \cdot \mathbf{r} | \Psi_k^v \rangle|^2 \delta(E_k^c - E_k^v - \hbar\omega) \quad (4)$$

In this expression, \mathbf{u} represents the polarization vector of the incident light, e is the elementary charge, and \hbar denotes the reduced Planck constant. The term $\langle \Psi_k^c | \mathbf{u} \cdot \mathbf{r} | \Psi_k^v \rangle$ corresponds to the transition matrix element utilizing the momentum operator $\mathbf{u} \cdot \mathbf{r}$. Furthermore, E_k^c and E_k^v designate the energy levels of the conduction and valence bands, respectively, at a given wave vector k , while ω is the angular frequency.

To evaluate the real component of the dielectric function, ϵ_1 , the Kramers–Kronig relation is applied [65]:

$$\epsilon_1(\omega) = 1 + \frac{2}{\pi} P \int_0^\infty \frac{\epsilon_2(\omega^*)\omega^*}{\omega^{*2} - \omega^2} d\omega^* \quad (5)$$

where P indicates the Cauchy principal value of the integral.

Based on these dielectric components, the material's optical absorption coefficient, α , can be computed using the following equation [66]:

$$\alpha(\omega) = \frac{4\pi\kappa(\omega)}{\lambda\sqrt{2}} \left(\sqrt{\epsilon_1^2(\omega) + \epsilon_2^2(\omega)} - \epsilon_1(\omega) \right)^{1/2} \quad (6)$$

where λ represents the wavelength of the light and κ stands for the extinction coefficient.

Finally, the frequency-dependent refractive index, $n(\omega)$, and extinction coefficient, $k(\omega)$, are directly derived from the real and imaginary parts of the dielectric function via the following expressions[66]:

$$n(\omega) = \frac{1}{\sqrt{2}} \left[\sqrt{\epsilon_1^2(\omega) + \epsilon_2^2(\omega)} + \epsilon_1(\omega) \right]^{1/2} \quad (7)$$

$$k(\omega) = \frac{1}{\sqrt{2}} \left[\sqrt{\epsilon_1^2(\omega) + \epsilon_2^2(\omega)} - \epsilon_1(\omega) \right]^{1/2} \quad (8)$$

The calculated optical properties of $\text{Cs}_3\text{Cu}_2\text{X}_5$ ($\text{X} = \text{Cl}, \text{Br}, \text{I}$) are illustrated in Fig. 6, including the real part of the refractive index (n), extinction coefficient (k), and absorption coefficient as functions of photon energy in the range of 0–20 eV.

Figure 6(a) presents the real part of the refractive index (n). In the low-energy region, all compounds exhibit relatively high static refractive indices, indicating strong polarization response. Prominent peaks in n are observed in the ultraviolet (UV) region, which originate from interband electronic transitions. Among the three compounds, noticeable variations in peak positions and magnitudes are observed, reflecting the influence of halogen substitution on the electronic polarizability and band structure.

The extinction coefficient (k), shown in Fig. 6(b), remains nearly zero in the low-energy region below the band gap, confirming the semiconducting nature of these materials. As the photon energy exceeds the band gap, k increases sharply due to the onset of interband transitions. Distinct peaks appear in the UV region, corresponding to strong optical transitions between the valence and conduction bands. The halogen-dependent shift in peak positions further demonstrates the tunability of optical response through chemical substitution.

Figure 6(c) shows how absorption varies with photon energy. The absorption edge lines up with the band gap for each compound, as expected from the electronic structure. All three absorb strongly in the UV with peaks around 10^5 cm^{-1} . The differences between $\text{Cs}_3\text{Cu}_2\text{Cl}_5$, $\text{Cs}_3\text{Cu}_2\text{Br}_5$, and $\text{Cs}_3\text{Cu}_2\text{I}_5$ come from how the orbitals mix and how the bands disperse when you change the halogen.

The optical spectra confirm strong UV transitions across the series. Changing the halide tunes the optical response. These characteristics suggest potential applications in ultraviolet optoelectronic and photonic devices.

3.2 Composition-Dependent Plasmonic Enhancement

Table 2 lists the optimized nanostructure dimensions and FDTD results for all three halides. $\text{Cs}_3\text{Cu}_2\text{Cl}_5$ has the highest Purcell factor ($4.4\times$) and LEE (30%), while $\text{Cs}_3\text{Cu}_2\text{Br}_5$ gives the best spectral overlap ($J_{\text{cos}} = 0.955$). $\text{Cs}_3\text{Cu}_2\text{I}_5$ falls behind on both metrics. The differences come down to how the optical constants of each material interact with the plasmon resonance. Lower refractive index helps the chloride, while the bromide benefits from better wavelength matching with the nanorod LSPR.

Table 2: FDTD results for plasmonic $\text{Cs}_3\text{Cu}_2\text{X}_5$ -based PeLEDs.

X	Composition	Emission λ (nm)	Nanostructure	Radius (nm)	Length (nm)	Purcell	Peak λ (nm)	LEE (%)	J_{\cos}
Cl	$\text{Cs}_3\text{Cu}_2\text{Cl}_5$	529	Nanorod	12	50	4.4	539	30	0.946
Br	$\text{Cs}_3\text{Cu}_2\text{Br}_5$	593	Nanorod	18	50	2.8	600	26	0.955
I	$\text{Cs}_3\text{Cu}_2\text{I}_5$	541	Nanosphere	15	—	2.4	538	10	0.846

$\text{Cs}_3\text{Cu}_2\text{Cl}_5$. Figure 7 shows the device-level performance for the $\text{Cs}_3\text{Cu}_2\text{Cl}_5$ -based LED. A $4.4\times$ Purcell enhancement is observed at 539 nm (Fig. 7a). This enhancement indicates faster spontaneous emission due to increased local density of optical states near the Ag nanorod surface. The relatively low refractive index of $\text{Cs}_3\text{Cu}_2\text{Cl}_5$ ($n \approx 1.9$ at 539 nm) reduces dielectric screening of the plasmonic near-field. This allows stronger coupling between the emitter dipole and the plasmon mode compared to the higher-index Br and I compositions.

The spectral overlap peaks at the same wavelength (Fig. 7b) with $J_{\cos} = 0.946$. This confirms good resonance matching between the emitter and the nanorod LSPR. Strong spectral alignment is important because Purcell enhancement depends on overlap between the emission spectrum and plasmonic mode density.

LEE goes from around 18% without the nanorod to 30% with it (Fig. 7c), a $1.7\times$ improvement. The plasmon scatters light that would otherwise remain trapped in waveguide and substrate modes, redirecting it into the far field. The LEE peak appears at slightly longer wavelengths than the Purcell peak. This offset occurs because near-field coupling and far-field scattering do not optimize at the same wavelength. Strong near-field enhancement requires tight mode confinement, while efficient extraction needs good scattering into propagating waves. These two requirements compete to some extent. Regardless, 30% extraction compares favorably to the 10–20% typical of perovskite LEDs without optical engineering.

The far-field pattern at 539 nm (Fig. 7d) is smooth and close to Lambertian. Most intensity falls within $\pm 60^\circ$ of normal, with no secondary lobes. This indicates that the nanorod functions as a scattering center rather than an antenna imposing narrow directionality. Such wide-angle emission is desirable for display applications where uniform brightness across viewing angles matters.

$\text{Cs}_3\text{Cu}_2\text{Br}_5$. The $\text{Cs}_3\text{Cu}_2\text{Br}_5$ -based LED shows $2.8\times$ Purcell enhancement at 600 nm (Fig. 8a). This is lower than $\text{Cs}_3\text{Cu}_2\text{Cl}_5$ even though the spectral overlap is the highest among all three compositions ($J_{\cos} = 0.955$, Fig. 8b). This can be explained by the higher refractive index of $\text{Cs}_3\text{Cu}_2\text{Br}_5$ ($n \approx 2.1$ at 600 nm). A higher index increases dielectric screening around the nanorod and reduces the effective near-field intensity at the emitter location. The Purcell factor scales roughly as $F_P \propto n^{-3}$, which explains the reduced enhancement in higher-index materials.

LEE improves from around 20% to 26% (Fig. 8c). This $1.3\times$ enhancement is more modest than for $\text{Cs}_3\text{Cu}_2\text{Cl}_5$. The higher refractive index increases the critical angle for total internal reflection. As a result, more photons remain trapped in substrate and waveguide modes. The extinction coefficient of $\text{Cs}_3\text{Cu}_2\text{Br}_5$ is also higher at the emission wavelength (Fig. 8b), leading to increased reabsorption losses.

The far-field pattern at 600 nm (Fig. 8d) is broader than that of $\text{Cs}_3\text{Cu}_2\text{Cl}_5$. More intensity appears at oblique angles. This broadening suggests that some emitted light couples to guided modes before being scattered out. The longer optical path associated with these guided modes also contributes to lower LEE.

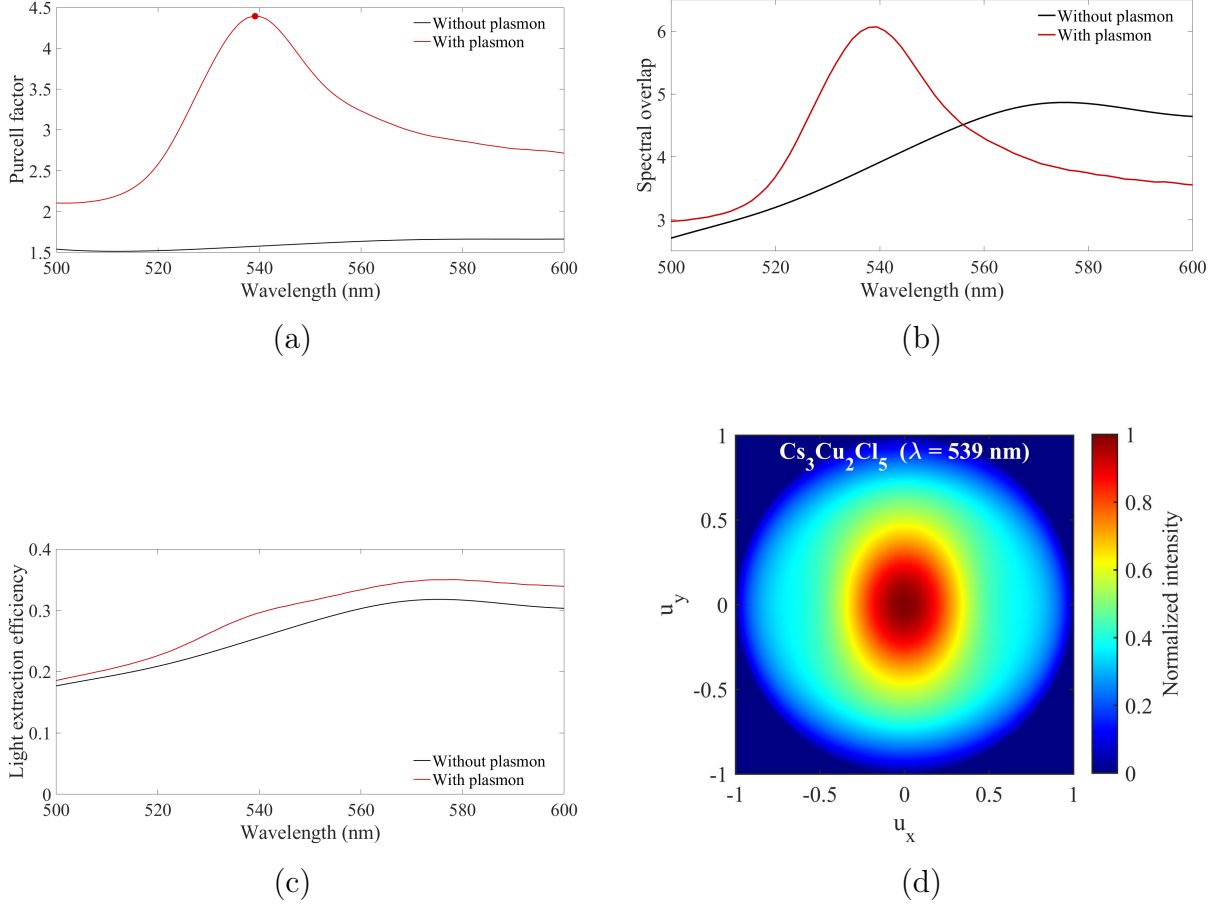


Figure 7: Device-level optical performance of the $\text{Cs}_3\text{Cu}_2\text{Cl}_5$ -based LED with optimized Ag/SiO_2 nanorod. (a) Purcell factor. (b) Spectral overlap. (c) Light extraction efficiency. (d) Far-field radiation pattern at 539 nm.

$\text{Cs}_3\text{Cu}_2\text{I}_5$. For $\text{Cs}_3\text{Cu}_2\text{I}_5$, a nanosphere geometry was used instead of a nanorod. Parametric optimization showed that nanorods could not achieve good spectral overlap with the $\text{Cs}_3\text{Cu}_2\text{I}_5$ emission at 541 nm. The different dielectric environment created by the iodide composition shifts the optimal LSPR condition. The isotropic field distribution of nanospheres provides better mode matching with the emission dipole orientation in this material.

The Purcell factor peaks at $2.4\times$ at 538 nm (Fig. 9a). This is the lowest among the three compositions. Without plasmonic coupling, the Purcell factor stays near 1.1 to $1.2\times$. This indicates weak cavity effects in the device stack at this emission wavelength. The spectral overlap is also the lowest ($J_{\cos} = 0.846$, Fig. 9b). This reflects limited alignment between the nanosphere LSPR and the emission spectrum.

LEE remains at only 10% (Fig. 9c). This is much lower than the Cl and Br compositions. The combination of high refractive index ($n \approx 2.2$) and substantial extinction coefficient at the emission wavelength promotes strong optical confinement and reabsorption. The far-field pattern (Fig. 9d) shows clear distortion with significant intensity at high angles. This confirms that many emitted photons couple to guided or substrate modes rather than escaping to free space.

The $\text{Cs}_3\text{Cu}_2\text{I}_5$ case shows a key limitation. Even with reasonable Purcell enhancement, extraction remains poor. Accelerating emission does not guarantee that photons escape

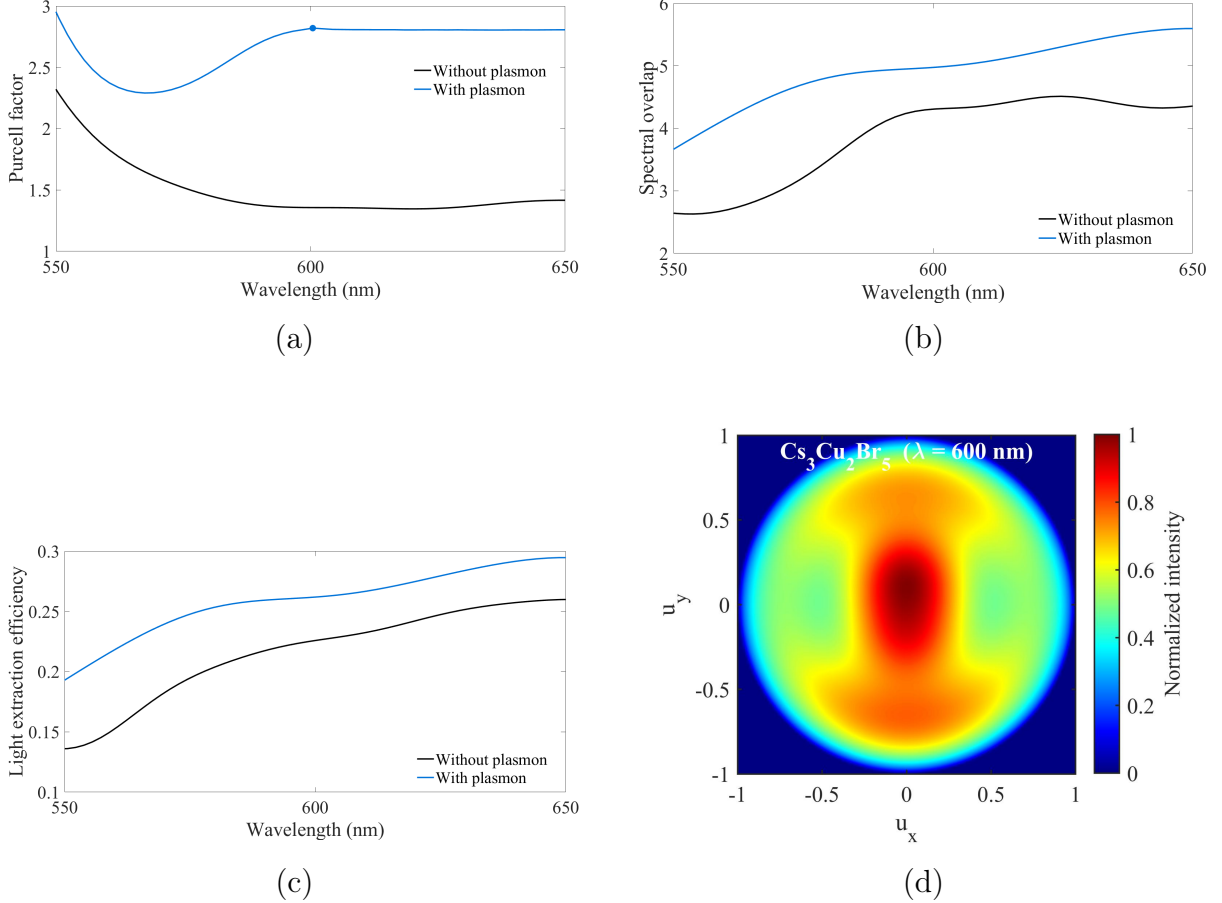


Figure 8: Device-level optical performance of the Cs₃Cu₂Br₅-based LED with optimized Ag/SiO₂ nanorod. (a) Purcell factor. (b) Spectral overlap. (c) Light extraction efficiency. (d) Far-field radiation pattern at 600 nm.

the device. The refractive index and extinction coefficient of the host set an upper bound on extraction, and plasmonic enhancement cannot fully compensate for a high-index environment.

3.3 Comparative Performance and Trade-Off Analysis

Figure 10 puts all three compositions side by side. The differences in plasmonic enhancement across the halide series tie directly to the DFT-derived optical constants, so comparing them together helps explain why some materials respond better than others.

Peak Enhancement Comparison. Figure 10(a) plots the peak enhancement values for each halide. Cs₃Cu₂Cl₅ leads with a 4.4× Purcell factor, 30% LEE, and 0.946 spectral overlap. The chloride does well because its refractive index is low ($n \approx 1.9$), which cuts down dielectric screening and lets the emitter couple more strongly to the nanorod near-field. The plasmonic field penetrates further into the active layer before getting damped. Cs₃Cu₂Br₅ and Cs₃Cu₂I₅ have higher indices, so the same nanorod geometry produces weaker enhancement in those hosts.

Cs₃Cu₂Br₅ exhibits moderate but balanced enhancement across all metrics. The higher refractive index ($n \approx 2.1$) limits the Purcell factor to 2.8× despite achieving the best spectral overlap (0.955). This shows that spectral matching alone cannot compensate for

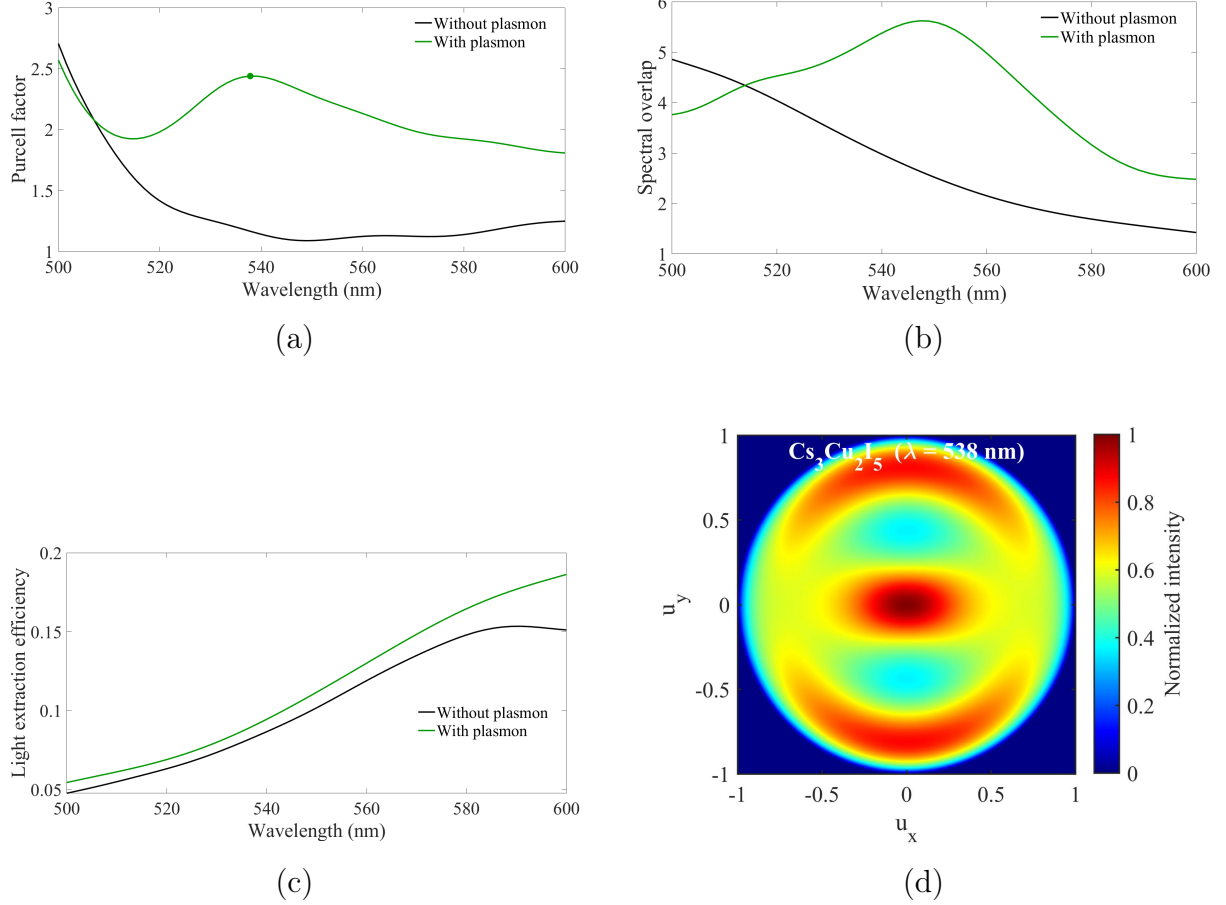


Figure 9: Device-level optical performance of the $\text{Cs}_3\text{Cu}_2\text{I}_5$ -based LED with optimized Ag/SiO_2 nanosphere. (a) Purcell factor. (b) Spectral overlap. (c) Light extraction efficiency. (d) Far-field radiation pattern at 538 nm.

increased dielectric losses in higher-index materials.

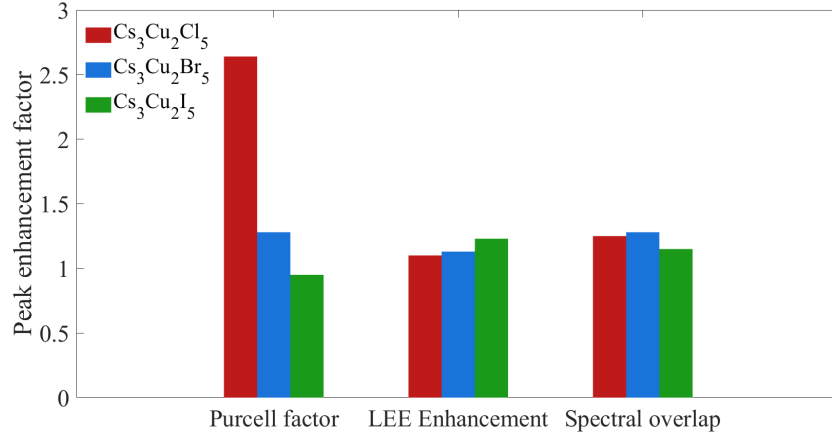
$\text{Cs}_3\text{Cu}_2\text{I}_5$ shows the weakest response with Purcell factor of $2.4\times$ and LEE of only 10%. The high refractive index ($n \approx 2.2$) and large extinction coefficient at the emission wavelength cause strong optical confinement. Even with a nanosphere geometry optimized for this composition, the spectral overlap remains limited at 0.846.

Purcell Factor and LEE Trade-Off. Figure 10(b) maps the relationship between peak Purcell factor and peak LEE. The shaded regions represent the accessible design space for each composition through nanostructure geometry optimization.

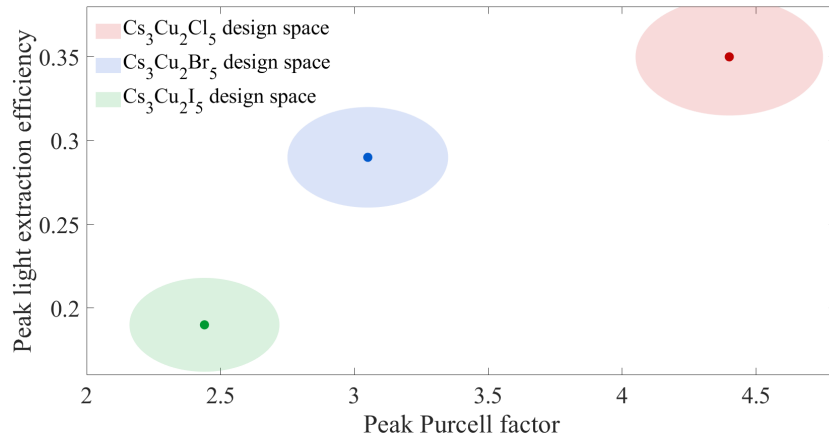
$\text{Cs}_3\text{Cu}_2\text{Cl}_5$ occupies the upper-right region where both high Purcell factor and high LEE are achievable. This is because the low refractive index creates favourable conditions for both near-field enhancement and far-field extraction. The plasmonic near-field is less screened, and the critical angle for total internal reflection is larger. Both effects work together to improve device performance.

$\text{Cs}_3\text{Cu}_2\text{Br}_5$ lies in an intermediate region. The higher index material can still achieve reasonable Purcell enhancement through geometry optimization. However, the increased optical confinement limits how much of this enhanced emission can be extracted to the far field.

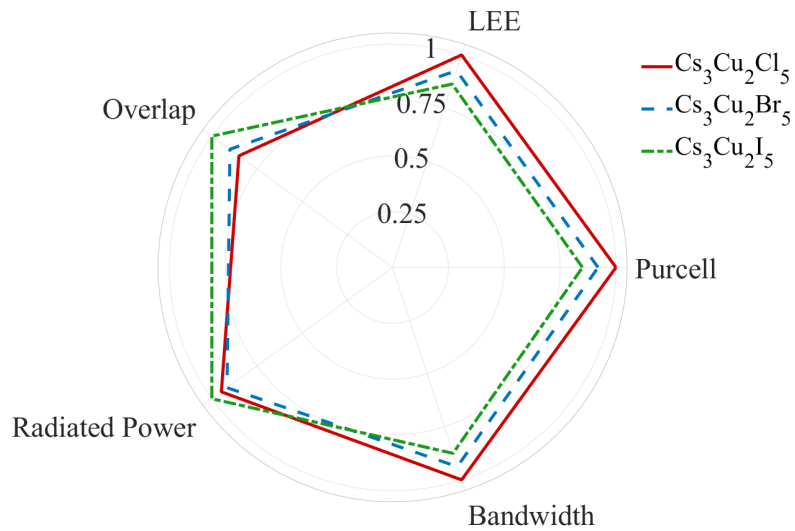
$\text{Cs}_3\text{Cu}_2\text{I}_5$ is confined to the lower-left region. The high refractive index creates a fundamental trade-off. Stronger near-field confinement could increase the Purcell factor,



(a)



(b)



(c)

Figure 10: Comparative performance of plasmon-enhanced $\text{Cs}_3\text{Cu}_2\text{X}_5$ -based LEDs. (a) Peak enhancement factors for Purcell factor, LEE, and spectral overlap. (b) Purcell factor and LEE trade-off map showing the design space for each composition. (c) Radar plot comparing normalized performance metrics across the halide series.

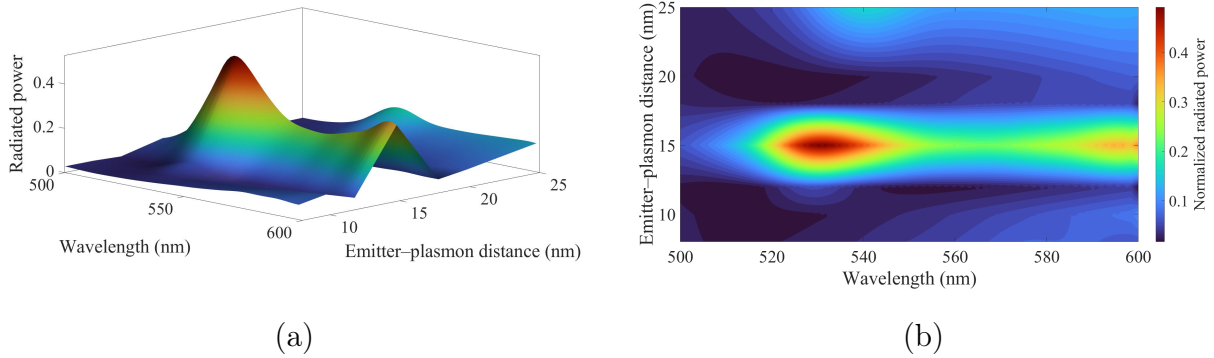


Figure 11: Distance and wavelength dependent radiated power for the $\text{Cs}_3\text{Cu}_2\text{Cl}_5$ -based LED. (a) 3D surface plot showing a localized maximum at around 15 nm separation and 530 to 540 nm wavelength. (b) 2D contour map showing the narrow optimal coupling window.

but this same confinement traps more light inside the device. The design space is therefore limited by the intrinsic optical properties of the material rather than by the plasmonic structure.

This points to a key design consideration. For plasmon-enhanced LEDs, the choice of emitter material matters as much as the nanostructure geometry. A high Purcell factor in a high-index host may not improve device efficiency if most photons remain trapped.

Multi-Parameter Summary. Figure 10(c) shows a normalized radar plot covering four performance metrics. $\text{Cs}_3\text{Cu}_2\text{Cl}_5$ has the largest area, meaning it performs well across Purcell factor, LEE, radiated power, and bandwidth. The balanced shape indicates that plasmonic enhancement and light extraction work together effectively in this material.

$\text{Cs}_3\text{Cu}_2\text{Br}_5$ has a smaller but still balanced profile. All metrics drop compared to $\text{Cs}_3\text{Cu}_2\text{Cl}_5$, which follows from the higher refractive index weakening both near-field coupling and far-field extraction.

$\text{Cs}_3\text{Cu}_2\text{I}_5$ has the smallest area, with LEE and radiated power particularly low. The shape is also uneven since spectral overlap stays reasonable while extraction suffers. This confirms that optical confinement limits the iodide more than the other two compositions.

Among the $\text{Cs}_3\text{Cu}_2\text{X}_5$ series, $\text{Cs}_3\text{Cu}_2\text{Cl}_5$ stands out as the best candidate for plasmon-enhanced LEDs. Its low refractive index and strong plasmonic coupling together offer a route to better device efficiency.

3.4 Dependence of Radiated Power on Wavelength and Emitter-Plasmon Distance

Radiated power was mapped against wavelength and emitter-plasmon distance to see how near-field coupling turns into usable light output. This also clarifies why a 5 nm SiO_2 shell works best. Fig. 11 and Fig. 12 show the results for $\text{Cs}_3\text{Cu}_2\text{Cl}_5$ and $\text{Cs}_3\text{Cu}_2\text{Br}_5$, respectively. Both figures include a 3D surface plot and a 2D contour map.

$\text{Cs}_3\text{Cu}_2\text{Cl}_5$. Figure 11 shows the radiated power distribution for the $\text{Cs}_3\text{Cu}_2\text{Cl}_5$ -based LED. A clear maximum appears at around 530 to 540 nm wavelength and 15 nm emitter-plasmon separation.

The sharp peak in Fig. 11(a) indicates that efficient near-field to far-field conversion occurs only within a narrow distance window. This behaviour arises from the competition

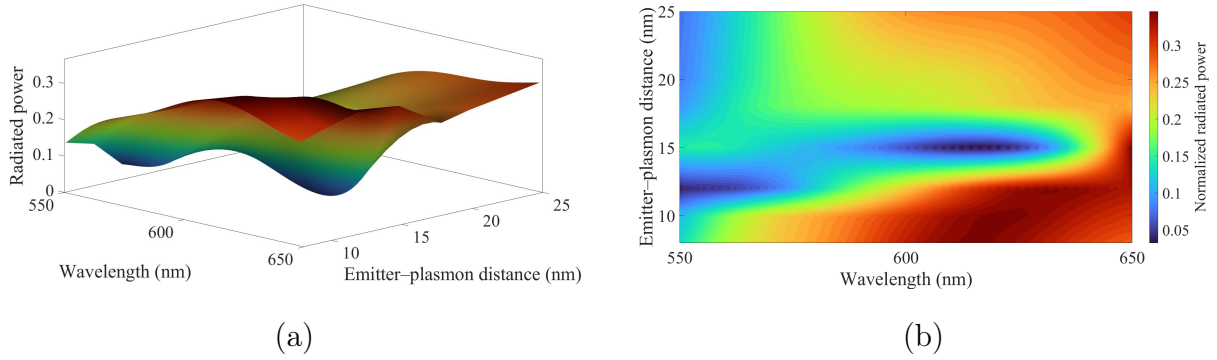


Figure 12: Distance and wavelength dependent radiated power for the $\text{Cs}_3\text{Cu}_2\text{Br}_5$ -based LED. (a) 3D surface plot showing a broader maximum compared to $\text{Cs}_3\text{Cu}_2\text{Cl}_5$. (b) 2D contour map revealing a dark band at 14 to 16 nm and secondary enhancement at around 25 nm.

between two effects. At short distances below 10 nm, the emitter couples strongly to the plasmonic near-field. However, this strong coupling also opens non-radiative decay channels through energy transfer to the metal. The energy is then dissipated as heat in the Ag core rather than being radiated to the far field. At longer distances above 20 nm, the near-field intensity decays exponentially and coupling becomes too weak to provide significant enhancement.

The optimal distance of around 15 nm represents a balance between these competing effects. At this separation, the emitter experiences strong field enhancement while remaining outside the dominant quenching zone. The contour plot in Fig. 11(b) shows a bright horizontal band at this distance across the 520 to 560 nm wavelength range. The narrow spectral width of this band reflects the resonant nature of plasmonic enhancement. Maximum radiation occurs when the emission wavelength matches both the LSPR and the optimal coupling distance simultaneously.

The 5 nm SiO_2 shell thickness used in this work places the perovskite emitter layer at approximately 10 to 20 nm from the Ag core surface, depending on dipole position within the active layer. This range falls within the optimal coupling window identified in Fig. 11(b), validating the shell design choice.

$\text{Cs}_3\text{Cu}_2\text{Br}_5$. Figure 12 shows the radiated power distribution for $\text{Cs}_3\text{Cu}_2\text{Br}_5$. The behaviour is notably different from $\text{Cs}_3\text{Cu}_2\text{Cl}_5$. The optimal coupling region is shifted to shorter distances of 8 to 12 nm and longer wavelengths of 620 to 650 nm.

The shift to shorter optimal distance can be explained by the higher refractive index of $\text{Cs}_3\text{Cu}_2\text{Br}_5$. The plasmonic near-field decays faster in higher-index media because the field penetration depth scales inversely with refractive index. To maintain strong coupling, the emitter must be placed closer to the metal surface. However, this also increases the risk of non-radiative quenching.

A dark band shows up at 14 to 16 nm in the contour plot of Fig. 12(b). In this range, the emitter sits too far from the metal for strong plasmonic coupling, but not far enough to radiate efficiently on its own. The high refractive index still traps much of the light through total internal reflection.

A secondary enhancement region appears around 25 nm. At this distance, plasmonic coupling weakens and the emitter behaves more like a free dipole in a layered stack. Less interaction with the metal reduces non-radiative losses, allowing some light to escape

through standard outcoupling rather than plasmon-mediated scattering. However, this secondary peak is broader and weaker than the primary one, indicating that plasmonic enhancement remains the more efficient extraction path.

This more complex distance dependence is why $\text{Cs}_3\text{Cu}_2\text{Br}_5$ ends up with lower LEE (26%) than $\text{Cs}_3\text{Cu}_2\text{Cl}_5$ (30%), even though their spectral overlap is similar. The tighter optimal coupling window combined with stronger optical confinement makes efficient extraction harder to maintain across the full active layer.

Design Implications. This distance-dependent analysis provides important guidance for device fabrication. For $\text{Cs}_3\text{Cu}_2\text{Cl}_5$, the optimal emitter-plasmon separation of around 15 nm allows some flexibility in shell thickness and emitter positioning. For $\text{Cs}_3\text{Cu}_2\text{Br}_5$, the tighter optimal window of 8 to 12 nm requires more precise control over nanostructure placement. These constraints should be considered when translating the simulation results to experimental device fabrication.

3.5 Experimental Validation and Fabrication Outlook

The calculated emission wavelengths agree well with experimental reports. $\text{Cs}_3\text{Cu}_2\text{Cl}_5$ emits at 525–526 nm in photoluminescence measurements,[67, 68] consistent with our simulations. PLQYs approaching 100% have been reported for $\text{Cs}_3\text{Cu}_2\text{Cl}_5$ and 97% for $\text{Cs}_3\text{Cu}_2\text{I}_5$ with optimized synthesis,[69, 70] confirming that these materials are intrinsically efficient emitters.

Table 3: Comparison of plasmonic enhancement in perovskite light-emitting systems.

Plasmonic structure	Emitter	Enhancement	Ref.
Ag nanocubes	CsPbBr_3 QDs	$3.5\times$ PL, $4.5\times$ rate	[71]
Ag nanowire network	CsPbBr_3 QDs	$6\times$ PL	[72]
Au NPs in PEDOT:PSS	CsPbBr_3	$3.8\times$ PL	[73]
Ag/ SiO_2 nanorod	$\text{Cs}_3\text{Cu}_2\text{Cl}_5$	$4.4\times$ Purcell	This work
Ag/ SiO_2 nanorod	$\text{Cs}_3\text{Cu}_2\text{Br}_5$	$2.8\times$ Purcell	This work
Ag/ SiO_2 nanosphere	$\text{Cs}_3\text{Cu}_2\text{I}_5$	$2.4\times$ Purcell	This work

Functional $\text{Cs}_3\text{Cu}_2\text{X}_5$ -based LEDs have been demonstrated. Jun et al. reported $\text{Cs}_3\text{Cu}_2\text{I}_5$ blue LEDs with maximum luminance of 10 cd/m^2 using thermal evaporation.[74] Liu et al. achieved 70 cd/m^2 and 0.1% EQE.[75] More recent work on mixed-phase copper halide LEDs reached 0.8% EQE.[76] The Cu^+ oxidation state provides excellent ambient stability, with films maintaining optical properties for months without encapsulation.[68]

The predicted Purcell enhancement values are comparable to other plasmon-enhanced perovskite systems (Table 3). Ag nanocube arrays coupled with perovskite quantum dots achieved 3.5-fold fluorescence intensity and 4.5-fold emission rate enhancement.[71] Ag nanowire networks demonstrated up to 6-fold enhancement.[72] Au nanoparticles in PEDOT:PSS showed 3.8-fold PL improvement in blue perovskite LEDs.[73] Our predicted LEE also exceeds the 10–20% typical of standard perovskite LEDs.[12]

Ag/ SiO_2 core-shell nanoparticles have been successfully integrated into perovskite solar cells. He et al. showed that Ag@SiO_2 with 5 nm shell thickness improved PCE by 16%.[77] Wang et al. demonstrated Ag@SiO_2 nanowires achieving 18% PCE.[78] The SiO_2 shell prevents charge transfer to the metal while preserving near-field coupling.

Several fabrication challenges should be noted. Precise nanoparticle positioning within the device stack remains difficult. Solution-processed deposition may yield non-uniform

distribution, reducing the average enhancement below simulated values. Nevertheless, both $\text{Cs}_3\text{Cu}_2\text{X}_5$ films and Ag/SiO_2 nanoparticles can be synthesized using established methods, suggesting experimental realization is feasible.

4 Conclusions

An integrated DFT-FDTD framework has been developed to investigate plasmon-enhanced light extraction in lead-free $\text{Cs}_3\text{Cu}_2\text{X}_5$ ($X = \text{Cl}, \text{Br}, \text{I}$) LEDs. First-principles calculations provided composition-specific optical constants that were directly implemented in device-level FDTD simulations for nanostructure optimization.

Among the three compositions studied, $\text{Cs}_3\text{Cu}_2\text{Cl}_5$ exhibits the best overall performance with $4.4\times$ Purcell enhancement, 30% light extraction efficiency, and near-Lambertian far-field emission. This superior response originates from the lower refractive index of the material, which reduces dielectric screening and enables stronger near-field coupling with the plasmonic nanorod. $\text{Cs}_3\text{Cu}_2\text{Br}_5$ achieves the highest spectral overlap (0.955) but yields only moderate extraction efficiency (26%) due to increased optical confinement. $\text{Cs}_3\text{Cu}_2\text{I}_5$ exhibits the weakest response with extraction efficiency limited to 10%. This result demonstrates that Purcell enhancement alone does not ensure efficient light extraction in high-index host materials.

The distance analysis shows that optimal coupling conditions depend on composition. $\text{Cs}_3\text{Cu}_2\text{Cl}_5$ has a wider tolerance window with best performance near 15 nm, while $\text{Cs}_3\text{Cu}_2\text{Br}_5$ needs tighter control at 8–12 nm. These differences matter for experimental device fabrication.

Some limitations should be noted. The simulations assume high internal quantum efficiency and do not include non-radiative recombination or defect losses. The reported values therefore represent optical upper bounds. Real device performance will depend on material quality and defect passivation. Ohmic losses in the metal nanostructures also create a trade-off between radiative enhancement and absorption, which requires careful spacer design.

The results show that optical design for plasmon-enhanced lead-free LEDs needs to account for composition. The combination of chemical stability, high intrinsic quantum yield, and strong plasmonic coupling identifies $\text{Cs}_3\text{Cu}_2\text{Cl}_5$ as a promising candidate for next-generation light-emitting applications. Experimental validation through fabrication of plasmon-integrated $\text{Cs}_3\text{Cu}_2\text{X}_5$ devices represents the logical next step.

Author contributions

Shoumik Debnath: Conceptualization, Methodology, Software, Validation, Formal analysis, Investigation, Data curation, Writing – original draft, Writing – review & editing, Visualization. **Sudipta Saha:** Methodology, Software, Validation, Formal analysis, Writing – review & editing. **Khondokar Zahin:** Methodology, Validation, Data curation, Writing – review & editing. **Ying Yin Tsui:** Writing – review & editing, Supervision, Project administration. **Md. Zahurul Islam:** Conceptualization, Resources, Writing – review & editing, Supervision, Project administration.

Conflicts of interest

There are no conflicts to declare.

Data availability

Representative FDTD simulation files supporting this study are available on GitHub at https://github.com/debnath-shoumik/PeLED_FDTD_Cs3Cu2X5. All remaining data are available from the corresponding author upon reasonable request.

Acknowledgement

The authors acknowledge the financial support provided by the Basic Research Grant, Bangladesh University of Engineering and Technology (BUET), under Office Order No.: Shongstha/R-60/Re-2413, dated 10 October 2023 (Professor Dr. Md. Zahurul Islam). The authors also acknowledge the logistical support provided by the Department of Electrical and Electronic Engineering (EEE), BUET, throughout the duration of this work.

References

- [1] L. Kong, Y. Sun, B. Zhao, K. Ji, J. Feng, J. Dong, Y. Wang, Z. Liu, S. Maqbool, Y. Li, Y. Yang, L. Dai, W. Lee, C. Cho, S.D. Stranks, R.H. Friend, N. Wang, N.C. Greenham, and X. Yang. Fabrication of red-emitting perovskite leds by stabilizing their octahedral structure. *Nature*, 631:73–79, 2024.
- [2] C.C. Li, T. Yu Huang, Y.H. Lai, Y.C. Huang, and C. Shan Tan. Lead-free perovskites for flexible optoelectronics. *Materials Today Electronics*, 8, 2024.
- [3] Y. Nong, J. Yao, J. Li, L. Xu, Z. Yang, C. Li, and J. Song. Boosting external quantum efficiency of blue perovskite qleds exceeding 23% by trifluoroacetate passivation and mixed hole transportation design. *Advanced Materials*, 36, 2024.
- [4] C. Cho, Y. Sun, J. You, L.S. Cui, and N.C. Greenham. Enhanced photon recycling enables efficient perovskite light-emitting diodes. *Advanced Functional Materials*, 34, 2024.
- [5] M. Li, Y. Yang, Z. Kuang, C. Hao, S. Wang, F. Lu, Z. Liu, J. Liu, L. Zeng, Y. Cai, Y. Mao, J. Guo, H. Tian, G. Xing, Y. Cao, C. Ma, N. Wang, Q. Peng, L. Zhu, W. Huang, and J. Wang. Acceleration of radiative recombination for efficient perovskite leds. *Nature*, 630:631–635, 2024.
- [6] C. Ma, M. Ni, X. Liu, K. Zhan, M. Chen, S. Li, F. Li, H. Wang, and Y. Dang. Recent progress in perovskite light-emitting diodes with high external quantum efficiency and stability. *CrystEngComm*, 27:3853–3876, 2025.
- [7] Y. Xiao, Q. Xue, X. Liu, F. Gao, and G. Xie. Lead-free perovskite leds powered by cyanuric acid. *Innovation*, 5, 2024.

- [8] D. Yang, B. Zhao, T. Yang, R. Lai, D. Lan, R.H. Friend, and D. Di. Toward stable and efficient perovskite light-emitting diodes. *Advanced Functional Materials*, 32, 2022.
- [9] I. López-Fernández, D. Valli, C.Y. Wang, S. Samanta, T. Okamoto, Y.T. Huang, K. Sun, Y. Liu, V.S. Chirvony, A. Patra, J. Zito, L. De Trizio, D. Gaur, H.T. Sun, Z. Xia, X. Li, H. Zeng, I. Mora-Seró, N. Pradhan, J.P. Martínez-Pastor, P. Müller-Buschbaum, V. Biju, T. Debnath, M. Saliba, E. Debroye, R.L.Z. Hoyer, I. Infante, L. Manna, and L. Polavarapu. Lead-free halide perovskite materials and optoelectronic devices: Progress and prospective. *Advanced Functional Materials*, 34, 2024.
- [10] L. Zhang, C. Sun, T. He, Y. Jiang, J. Wei, Y. Huang, and M. Yuan. High-performance quasi-2d perovskite light-emitting diodes: from materials to devices. *Light: Science & Applications*, 10, 2021.
- [11] J. Chen, H. Xiang, J. Wang, R. Wang, Y. Li, Q. Shan, X. Xu, Y. Dong, C. Wei, and H. Zeng. Perovskite white light emitting diodes: Progress, challenges, and opportunities. *ACS Nano*, 15:17150–17174, 2021.
- [12] B. Zhao, M. Vasilopoulou, A. Fakharuddin, F. Gao, A.R. bin Mohd Yusoff, R.H. Friend, and D. Di. Light management for perovskite light-emitting diodes. *Nature Nanotechnology*, 18:981–992, 2023.
- [13] C. Liu, B. Li, and M. Qiu. Advancements in the improvement of optical outcoupling efficiency for perovskite leds. *Advanced Devices and Instrumentation*, 5, 2024.
- [14] S. Rahimi, M. Eskandari, and D. Fathi. New nanostructure perovskite-based light-emitting diode with superior light extraction efficiency enhancement. *Scientific Reports*, 14, 2024.
- [15] S. Kar, N.F. Jamaludin, N. Yantara, S.G. Mhaisalkar, and W.L. Leong. Recent advancements and perspectives on light management and high performance in perovskite light-emitting diodes. *Nanophotonics*, 10:2103–2143, 2021.
- [16] H. Wang, A. Treglia, M.D. Albaqami, F. Gao, and A. Petrozza. Tin-halide perovskites for near-infrared light-emitting diodes. *ACS Energy Letters*, 9:2500–2507, 2024.
- [17] M. Zhang, X. Ma, J.L. Esguerra, H. Yu, O. Hjelm, J. Li, and F. Gao. Towards sustainable perovskite light-emitting diodes. *Nature Sustainability*, 8:315–324, 2025.
- [18] Md Faiaad Rahman, Arpan Sur, and Ahmed Zubair. Hierarchically structured and thermally robust perovskite solar cells with band-engineered double-hole layers. *Solar Energy Materials and Solar Cells*, 299:114201, 2026.
- [19] X.B. Shi, Y. Liu, Z. Yuan, X.K. Liu, Y. Miao, J. Wang, S. Lenk, S. Reineke, and F. Gao. Optical energy losses in organic–inorganic hybrid perovskite light-emitting diodes. *Advanced Optical Materials*, 6, 2018.
- [20] Q. Zhang, D. Zhang, Y. Fu, S. Poddar, L. Shu, X. Mo, and Z. Fan. Light outcoupling management in perovskite leds—what can we learn from the past? *Advanced Functional Materials*, 30, 2020.

- [21] M.H. Futscher and B. Ehrler. Modeling the performance limitations and prospects of perovskite/si tandem solar cells under realistic operating conditions. *ACS Energy Letters*, 2:2089–2095, 2017.
- [22] C. Chen, Y. Chen, Z. Fang, R. Ge, J. Wu, and X. Chen. Hybrid material integration for active photonic applications. *APL Photonics*, 9, 2024.
- [23] S. Zainab, M. Azeem, S.U. Awan, S. Rizwan, N. Iqbal, and J. Rashid. Optimization of bandgap reduction in 2-dimensional go nanosheets and nanocomposites of go/iron-oxide for electronic device applications. *Scientific Reports*, 13:6954, 2023.
- [24] P. Akhter, M. Huang, W. Spratt, N. Kadakia, and F. Amir. Tailoring the optical constants in single-crystal silicon with embedded silver nanostructures for advanced silicon photonics applications. *Journal of Applied Physics*, 117, 2015.
- [25] Q.-H. Yang, H.-Q. Wei, G.-H. Li, J.-B. Huang, X. Liu, and G.-M. Cai. Recent developments of lead-free halide-perovskite $\text{cs}_3\text{cu}_2\text{x}_5$ ($\text{x} = \text{cl}, \text{br}, \text{i}$): Synthesis, modifications, and applications. *Materials Today Physics*, 36:101143, 2023.
- [26] J. Li, Y. Ren, Z. Wang, and X. Li. Copper-based halide $\text{cs}_3\text{cu}_2\text{i}_5$: (x) bulk single crystals: Growth and applications. *Radiation Measurements*, 189:107527, 2025.
- [27] L. Lian, M. Zheng, P. Zhang, Z. Zheng, K. Du, W. Lei, J. Gao, G. Niu, D. Zhang, T. Zhai, S. Jin, J. Tang, X. Zhang, and J. Zhang. Photophysics in $\text{cs}_3\text{cu}_2\text{x}_5$ ($\text{x} = \text{cl}, \text{br}$, or i): Highly luminescent self-trapped excitons from local structure symmetrization. *Chemistry of Materials*, 32:3462–3468, 2020.
- [28] Y. Li, P. Vashishtha, Z. Zhou, Z. Li, S.B. Shivarudraiah, C. Ma, J. Liu, K.S. Wong, H. Su, and J.E. Halpert. Room temperature synthesis of stable, printable $\text{cs}_3\text{cu}_2\text{x}_5$ ($\text{x} = \text{i}, \text{br}/\text{i}, \text{br}, \text{br}/\text{cl}, \text{cl}$) colloidal nanocrystals with near-unity quantum yield green emitters ($\text{x} = \text{cl}$). *Chemistry of Materials*, 32:5515–5524, 2020.
- [29] S. Yue, S.C. McGuire, H. Yan, Y.S. Chu, M. Cotlet, X. Tong, and S.S. Wong. Synthesis, characterization, and stability studies of ge-based perovskites of controllable mixed cation composition, produced with an ambient surfactant-free approach. *ACS Omega*, 4:18219–18233, 2019.
- [30] F. Gao and C. Liu. Inorganic modification all-inorganic $\text{cs}_3\text{cu}_2\text{i}_5$ nanocrystals with near-unity deep-blue luminescence. 2025.
- [31] Z. Jiang, H. Liu, J. Zou, Y. Huang, Z. Xu, D. Pustovy, and S. Vitusevich. Scale-up synthesis of high-quality solid-state-processed cscux ($\text{x} = \text{cl}, \text{br}, \text{i}$) perovskite nanocrystal materials toward near-ultraviolet flexible electronic properties. *RSC Advances*, 13:5993–6001, 2023.
- [32] Y. Wang, X. Wen, P. Ran, C. Peng, F. Yang, Y. Yang, and Y. Wu. Efficient and stable 0d $\text{cs}_3\text{cu}_2\text{br}_5\text{:mn}$ single crystals for low-dose high-resolution x-ray imaging. *Laser & Photonics Reviews*, 19, 2025.
- [33] C. Liu, L. Wang, F. Fang, Z. Zhao, J. Pan, J. Akram, S. Bin Shafie, R.Z. Talaighila, Q. Li, Z. Zhao, J. Wu, Z. Zhu, W. Lei, X. Zhang, and J. Chen. Energy down-conversion $\text{cs}_3\text{cu}_2\text{cl}_5$ nanocrystals for boosting the efficiency of uv photodetector. *Frontiers in Materials*, 8, 2021.

- [34] X. Wen, Q. Gao, Q. Wang, W. Chewpraditkul, M. Korjik, S. Kurosawa, M. Buryi, V. Babin, and Y. Wu. Highly efficient in(i) doped cs₃cu₂i₅ single crystals for light-emitting diodes and gamma spectroscopy applications. *Optical Materials: X*, 23:100335, 2024.
- [35] B. Zhang, X. Wu, S. Zhou, G. Liang, and Q. Hu. Self-trapped exciton emission in inorganic copper(i) metal halides. *Frontiers of Optoelectronics*, 14:459–472, 2021.
- [36] D.-Y. Kim, J.-G. Jung, Y.-J. Lee, and M.-H. Park. Lead-free halide perovskite nanocrystals for light-emitting diodes. *Materials*, 16:6317, 2023.
- [37] H. Li, Y. Zhao, J. Lu, J. Feng, J. Zhao, K. Lin, W. Feng, L. Jiang, Z. Wei, Z. Du, and Y. Wu. Phase engineering reinforced energy transfer for high-performance blue perovskite light-emitting diodes. *Small*, 20, 2024.
- [38] P. Xiong, J.B. Liao, Z.Y. Wang, Q.H. Zuo, Y. Dai, J. Wu, and C.J. Tong. First-principles study on electronic and optical properties of perovskite light-emitting diodes cspb(br_{1-x}ix)₃. *Applied Physics Letters*, 126, 2025.
- [39] C.F. Ramirez-Gutierrez, H.D. Martinez-Hernandez, I.A. Lujan-Cabrera, and M.E. Rodriguez-García. Design, fabrication, and optical characterization of one-dimensional photonic crystals based on porous silicon assisted by in-situ photoacoustics. *Scientific Reports*, 9:14732, 2019.
- [40] N. Tabibifar, M. Eskandari, F.A. Boroumand, D. Fathi, and S. Rahimi. Enhanced light extraction by optimizing near-infrared perovskite-based light emitting diode (peled). *Scientific Reports*, 14, 2024.
- [41] X. Ma, N. Youngblood, X. Liu, Y. Cheng, P. Cunha, K. Kudtarkar, X. Wang, and S. Lan. Engineering photonic environments for two-dimensional materials. *Nanophotonics*, 10:1031–1058, 2021.
- [42] J. Bueno, A. Jiménez-Solano, M. Anaya, and S. Carretero-Palacios. Plasmonic nanoparticles boost low-current perovskite leds governed by photon recycling effects. *RSC Advances*, 15:32497–32508, 2025.
- [43] M. ul Ain, N. Asma, R. Ullah, Z. Fatima, A. Illahi, and W. Ahmed. Engineering gold nanoworms with tunable longitudinal plasmon peak in the near infrared and their refractive index sensing properties. *RSC Advances*, 14:12772–12780, 2024.
- [44] Y. Li, T. Gao, Z. He, C. Shen, S. Zhou, M. Li, D. Zhang, Q. Zhang, Y. Fu, X. Mo, Z. Zhang, W. Bi, and Z. Fan. Flexible perovskite light-emitting diodes: recent progress, applications and challenges. *npj Flexible Electronics*, 9, 2025.
- [45] J. Wen, K. Rong, L. Jiang, C. Wen, B. Wu, B. Sa, Y. Qiu, and R. Ahuja. Copper-based perovskites and perovskite-like halides: A review from the perspective of molecular level. *Nano Energy*, 128:109802, 2024.
- [46] J.S. Googasian and S.E. Skrabalak. Practical considerations for simulating the plasmonic properties of metal nanoparticles. *ACS Physical Chemistry Au*, 3:252–262, 2023.

- [47] A. Taflove, S.C. Hagness, and M. Piket-May. Computational electromagnetics: The finite-difference time-domain method. In *The Electrical Engineering Handbook*, pages 629–670. Elsevier, 2005.
- [48] Z. Zhou, Y. Li, Z. Xing, H.H.Y. Sung, I.D. Williams, Z. Li, K.S. Wong, and J.E. Halpert. Rapid synthesis of bright, shape-controlled, large single crystals of $\text{Cs}_3\text{Cu}_2\text{X}_5$ for phase pure single ($x = \text{Br}, \text{Cl}$) and mixed halides ($x = \text{Br/Cl}$) as the blue and green components for printable white light-emitting devices. *Advanced Materials Interfaces*, 8, 2021.
- [49] F. Brivio, K.T. Butler, A. Walsh, and M. van Schilfgaarde. Relativistic quasiparticle self-consistent electronic structure of hybrid halide perovskite photovoltaic absorbers. *Physical Review B*, 89:155204, 2014.
- [50] E.D. Palik. *Handbook of Optical Constants of Solids*. Academic Press, San Diego, 1985.
- [51] A. Alnuaimi, I. Almansouri, and A. Nayfeh. Effect of mobility and band structure of hole transport layer in planar heterojunction perovskite solar cells using 2d tcad simulation. *Journal of Computational Electronics*, 15:1110–1118, 2016.
- [52] E.M. Purcell, H.C. Torrey, and R.V. Pound. Resonance absorption by nuclear magnetic moments in a solid. *Physical Review*, 69:37–38, 1946.
- [53] J.-P. Berenger. A perfectly matched layer for the absorption of electromagnetic waves. *Journal of Computational Physics*, 114:185–200, 1994.
- [54] Pascal Anger, Palash Bharadwaj, and Lukas Novotny. Enhancement and quenching of single-molecule fluorescence. *Phys. Rev. Lett.*, 96:113002, Mar 2006.
- [55] M. Chen, M.G. Ju, H.F. Garces, A.D. Carl, L.K. Ono, Z. Hawash, Y. Zhang, T. Shen, Y. Qi, R.L. Grimm, D. Pacifici, X.C. Zeng, Y. Zhou, and N.P. Padture. Highly stable and efficient all-inorganic lead-free perovskite solar cells with native-oxide passivation. *Nature Communications*, 10, 2019.
- [56] Ling Gu, Kai Wen, Qi Peng, et al. Surface-plasmon-enhanced perovskite light-emitting diodes. *Small*, 16:2001861, 2020.
- [57] M. E. Raypah, A. A. Ahmed, and A. F. Omar. Application of porous materials and structures for improving optical and thermal performance of inorganic and organic light-emitting diodes: A review. *Sens. Actuators A: Phys.*, 347:113966, 2022.
- [58] Gregory A. Wurtz, Paul R. Evans, William Hendren, et al. Molecular plasmonics with tunable exciton–plasmon coupling strength in j-aggregate hybridized Au nanorod assemblies. *Nano Lett.*, 7:1297–1303, 2007.
- [59] Pu Mao, Chang Liu, Xin Li, et al. Single-step-fabricated disordered metasurfaces for enhanced light extraction from LEDs. *Light Sci. Appl.*, 10:180, 2021.
- [60] J. H. Lee et al. Far-field radiation of photonic crystal organic light-emitting diode. *Opt. Express*, 13:5864–5870, 2005.

- [61] Z. Y. Ooi, A. Jiménez-Solano, K. Gałkowski, et al. Strong angular and spectral narrowing of electroluminescence in an integrated tamm-plasmon-driven halide perovskite led. *Nat. Commun.*, 15:5802, 2024.
- [62] Lingling Xie, Bingkun Chen, Fa Zhang, Ziheng Zhao, Xinxin Wang, Lijie Shi, Yue Liu, Lingling Huang, Ruibin Liu, Bingsuo Zou, et al. Highly luminescent and stable lead-free cesium copper halide perovskite powders for uv-pumped phosphor-converted light-emitting diodes. *Photonics Research*, 8(6):768–775, 2020.
- [63] Md Lokman Ali, Mithun Khan, Md Abdullah Al Asad, and Md Zahidur Rahaman. Highly efficient and stable lead-free cesium copper halide perovskites for optoelectronic applications: A dft based study. *Heliyon*, 9(8), 2023.
- [64] Xixi Zheng, Jinxin Huang, Yaoyu Liu, Tianyu Wang, Shiguo Han, Zongqi Wang, Bing Teng, and Shaohua Ji. Stable lead-free blue-emitting $\text{Cs}_3\text{Cu}_2\text{Br}_5$ single crystal with self-trap exciton emission for optoelectronics. *Advanced Photonics Research*, 3(4):2100289, 2022.
- [65] M Gajdoš, Kerstin Hummer, G Kresse, J Furthmüller, and FJPRB Bechstedt. Linear optical properties in the projector-augmented wave methodology. *Physical Review B—Condensed Matter and Materials Physics*, 73(4):045112, 2006.
- [66] Sudipta Saha, Arpan Sur, Labonno Saha, and Md Kawsar Alam. Investigating the optical and thermodynamic properties of 2d moge_2p_4 : Potential material for photothermal therapy. *Nano Select*, 6(11):e70028, 2025.
- [67] Yingying Li, Zhifeng Shi, Wenqiang Liang, Lintao Wang, Shan Li, Fei Zhang, Zhangzhuang Ma, Yang Wang, Yongzheng Tian, Di Wu, Xinjian Li, Yongtao Zhang, Chongxin Shan, and Xiaosheng Fang. Energy down-conversion $\text{Cs}_3\text{Cu}_2\text{Cl}_5$ nanocrystals for boosting the efficiency of UV photodetector. *Front. Mater.*, 8:682833, 2021.
- [68] Linyuan Lian, Meiying Zheng, Wenzhen Zhang, Lixin Yin, Xiangyu Du, Peng Zhang, Xuewu Zhang, Jun Gao, Daoli Zhang, Lei Gao, Guozhong Xing, and Jianbing Zhang. Efficient and reabsorption-free radioluminescence in $\text{Cs}_3\text{Cu}_2\text{I}_5$ nanocrystals with self-trapped excitons. *Adv. Sci.*, 7:2000195, 2020.
- [69] Xiangping Chen et al. Near-unity PLQY of $\text{Cs}_3\text{Cu}_2\text{X}_5$ ($X = \text{Cl}, \text{Br}$) for high-efficiency white light-emitting diodes with exceptional color quality. *Adv. Mater.*, page 2500083, 2025.
- [70] Dongxu Han, Hailong Shi, Weiming Ming, Canxing Zhou, Bin Ma, Babak Saber, Mao-Hua Du, Xiaojun Chen, and Qianbo Zheng. Deep-blue emissive $\text{Cs}_3\text{Cu}_2\text{I}_5$ perovskites nanocrystals with 96.6% quantum yield via InI_3 -assisted synthesis for light-emitting device and fluorescent ink applications. *Nano Energy*, 99:107391, 2022.
- [71] Haizhou Li, Xueqing Zheng, Yuan Liu, Zongzhi Zhang, and Tao Jiang. Purcell-enhanced spontaneous emission from perovskite quantum dots coupled to plasmonic crystal. *J. Phys. Chem. C*, 123:25359–25365, 2019.
- [72] Qing Li, Zizhen Xu, James R. McBride, and Tianquan Lian. Plasmonic-perovskite solar cells, light emitters, and sensors. *Microsyst. Nanoeng.*, 8:5, 2022.

- [73] L. Xu et al. Blue perovskite LED with Au NPs in PEDOT:PSS. *Microsyst. Nanoeng.*, 8:5, 2022. Cited as ref. 143 in Li et al. *Microsyst. Nanoeng.* 2022.
- [74] Toshihiro Jun, Kanghoon Sim, Shogo Iimura, Masato Sasase, Hayato Kamioka, Junghwan Kim, and Hideo Hosono. Lead-free highly efficient blue-emitting Cs₃Cu₂I₅ with 0D electronic structure. *Adv. Mater.*, 30:1804547, 2018.
- [75] Yang Liu, Yuan Jing, Jie Zhao, Qingqing Liu, and Zhiguo Xia. Vacuum dual-source thermal-deposited lead-free Cs₃Cu₂I₅ films with high photoluminescence quantum yield for deep-blue light-emitting diodes. *ACS Appl. Mater. Interfaces*, 12:52967–52975, 2020.
- [76] Xiaoping Wang, Haoran Chen, Huanpeng Zhang, Xiao Li, Cong Zou, Lixin Xu, and Bingqiang Cao. Enhanced performance of cesium copper halide nanocrystal light-emitting diodes via post-treatment induced phase regulation. *J. Cent. South Univ.*, 30:2977–2987, 2023.
- [77] Zhengkai He, Cong Zhang, Rong Meng, Xuan Luo, Miaomiao Chen, Hongwei Lu, and Yongming Yang. Influence of Ag@SiO₂ with different shell thickness on photoelectric properties of hole-conductor-free perovskite solar cells. *Nanomaterials*, 10:2364, 2020.
- [78] Ding Wang, Wesley Chan, Zhibin Zhang, Xiaoyu Zeng, Ziruo Hong, Yuxin Liu, Junliang Chang, Huagui Wang, Wenying Tao, and Yue Hao. Enhanced efficiency of perovskite solar cells by using core-ultrathin shell structure Ag@SiO₂ nanowires as plasmonic antennas. *Adv. Electron. Mater.*, 3:1700169, 2017.